Comparison of B-spline Surface and Free-form Deformation Geometry Control for Aerodynamic Optimization

Christopher Lee*, David Koo† and David W. Zingg‡

Institute for Aerospace Studies, University of Toronto

4925 Dufferin St., Toronto, Ontario, M3H 5T6, Canada

Two aerodynamic shape optimization geometry control methods, B-spline surface control and free-form deformation (FFD), are applied to three optimization problems and compared on the bases of optimal shape performance and problem setup ease of use. For both methods, the geometry is parameterized using B-spline surfaces, with mesh movement accomplished using an efficient integrated technique. Gradients for the optimization algorithm are computed using the adjoint method. The first problem is a wing twist optimization under inviscid, subsonic flow, achieving an elliptical load distribution. The second is a lift-constrained drag minimization of a wing under transonic flow based on the Reynolds-averaged Navier-Stokes (RANS) equations. The third involves lift-to-drag ratio maximization, based on the RANS equations, beginning from a classically-shaped blended wing-body aircraft and converging to a lifting-fuselage configuration. B-spline surface control is often found to result in slightly better performance; however in general both methods perform equally well. FFD provides a more general approach to problem setup, decoupling geometry control from parameterization. Overall, the results suggest that B-spline surface control is better suited for simple geometries such as wings, while FFD is better suited for complex geometries such as unconventional aircraft and for implementation with multistart algorithms and adaptive geometry control approaches.

*Currently Application Engineer, Exa Corporation.

†Currently Senior Engineer, CD-adapco.

‡Professor and Director, J. Armand Bombardier Foundation Chair in Aerospace Flight, Associate Fellow AIAA.

Nomenclature

$\mathcal{J}$	Objective function
$\mathcal{M}$	Mesh residuals
$\mathcal{N}$	B-spline basis function
$\mathcal{R}$	Flow residuals
$\mathbf{A}$	Displaced surface control-point coordinates
$\mathbf{B}$	General B-spline coordinates
$\mathbf{b}$	Volume control-point coordinate vector
$\mathbf{b}_{\text{srf}}^{(i)}$	Surface control-point coordinate vector at mesh movement increment i
$\mathbf{q}$	Flow variables
$\mathbf{v}$	Design variable vector
A	Area
c	Chord length
C_d, C_D	2D, 3D drag coefficient
C_l, C_L	2D, 3D lift coefficient
C_m, C_M	2D, 3D pitching moment coefficient
C_p	Pressure coefficient
M	Mach number
m	Total mesh movement increments
p	B-spline degree
Re	Reynolds number
T	B-spline knot vector
t	Sectional thickness
V	Volume
x, y, z	Cartesian coordinate directions
y^+	Nondimensional off-wall distance

Symbols

α	Angle of attack
$\boldsymbol{\xi} = \xi, \eta, \zeta$	Parametric coordinates
γ	Twist

I. Introduction

Growing concern over the negative impact of carbon emissions in the environment and the rise of jet fuel prices pressure aircraft manufacturers to prioritize minimizing fuel burn when designing new aircraft. One key focus of technology advancement is improving aerodynamic performance through drag minimization using computational fluid dynamics (CFD). On its own, a CFD solver can analyze a single, specific design, but by coupling the solver with an optimization algorithm and geometry parameterization and control tools, designers are able to perform aerodynamic shape optimization (ASO), in which a given aerodynamic shape, such as a wing, is iteratively re-designed and re-analyzed, moving towards an optimal shape.[1–10] The importance of highly efficient and accurate CFD and optimization algorithms for the success of ASO is obvious, but another key component of ASO is the technique used to control the shape of the geometry throughout the optimization. The geometry control method defines what shapes can actually be explored during the optimization. It must be flexible enough to handle both detailed local changes, such as airfoil section shape, and global shape changes, such as planform shape, to ensure the true optimum is achieved. As a result, much work has gone into developing and evaluating different geometry parameterization and control techniques.[?, 9, 11–25]

Although this is not typically done, we make a distinction between geometry parameterization and control. While the variables used to parameterize the geometry can be controlled directly, it can be advantageous to use a second set of design variables to control the variables that parameterize the geometry, thereby decoupling parameterization and control. For example, Anderson et al.[14] solve a set of discretized partial differential equations on a control grid surrounding the geometry to perturb the underlying surface. Another example is the two-level approach of Gagnon and Zingg,[15] further discussed below, which retains the geometry parameterization of Hicken and Zingg[16] but uses a different approach to geometry control.

Perhaps the most obvious approach to both geometry parameterization and control is the discrete approach, in which the grid nodes directly define the surface and are the design variables.[26] This provides good local control and the simplicity of being able to use the computational grid without any additional parameterization, but can suffer from high cost for a dense surface grid, poor smoothness, and the absence of an analytical representation of the geometry.

The number of design variables can be reduced through the use of polynomial or spline approaches. In particular, B-spline curves are popular, since they can parametrize complex geometries efficiently and accurately and can also be used for geometry control through manipulation of control-point coordinates.[17] In addition, the more general non-uniform rational B-splines (NURBS) are able to define implicit conic sections exactly.[27]

Free-form deformation (FFD), first formally introduced by Sederberg and Parry,[28] can be visualized by embedding a flexible object of interest inside a flexible volume, and deforming both of them simultaneously by deforming the lattice of the volume. Since this is a volume-based parameterization, its applications can be extended to consider structural deformations in multidisciplinary design optimization. FFD is typically used as a method of geometry control and requires an underlying geometry parameterization; surface mesh nodes are often used for this purpose.

Another geometry control approach is the PARSEC method[18] which employs 11 parameters to define an airfoil. These parameters, such as leading-edge radius and trailing-edge angles, are of physical interest to designers, making this method popular for its intuitive concept, but it is overly restrictive for many applications.

The MASSOUD approach[19] also takes the approach of defining design variables such as thickness and camber, but parametrizes perturbations to the shape instead of the actual geometry. Analytical approaches add shape functions to a reference geometry. For example, Hicks-Henne "bump" functions[20] add weighted sine function perturbations to a baseline geometry to produce a new geometry. The Class function/Shape function Transformation (CST)[21] method defines geometries as a product of a class function defining the general geometry profile and a shape function defining key design parameters. The accuracy and flexibility of the CST method has been combined with the intuitiveness of the PARSEC method in a more recent airfoil parameterization technique.[22]

Proper orthogonal decomposition-based (POD) schemes take a training set of airfoils and generate a set of most important orthogonal shape modes to be used as design variables. The approach was introduced by Toal et al.[23] and has been used to reconstruct supercritical airfoils[29] and a larger range of airfoils, outperforming the Hicks-Henne "bump" functions and a linear approximation to the PARSEC method in a series of shape recovery studies.[30]

This is by no means a comprehensive list of all geometry control options available, and the reader is encouraged to consult Samareh[11] for more details.

Castonguay and Nadarajah[13] compared using mesh points, B-spline curves, Hicks-Henne bump functions, and the PARSEC method for airfoil design. For a viscous transonic inverse design case, mesh points and B-spline curves provided higher levels of accuracy. B-spline curves and Hicks-Henne bump functions were compared for lift-constrained drag minimization for the same case and showed comparable performance. A similar study was presented by Mousavi et al.[12] for a wing comparing mesh points, B-spline surfaces, and CST. B-spline surfaces and mesh points outperformed the CST method for both the inviscid transonic inverse design and drag minimization studies. Amoiralis and Nikolos[24] conducted a comparison between FFD and B-spline surface control and found that FFD generally led to a greater reduction of the cost function for a

comparable number of design variables for a series of inverse optimizations. The optimizations conducted, however, were two-dimensional inverse problems and used a low-fidelity solver.[31] Masters et al.[9] compared B-splines, Bezier surface FFD, CST, Hicks-Henne, a radial basis function domain element approach, and a POD method, applying the methods to the drag minimization of a NACA0012 airfoil in inviscid flow at zero angle of attack at Mach 0.85, with the constraint that the airfoil could only be thickened. The ability to ensure smooth geometries was shown to be a key requirement for faster optimization convergence, and the B-spline approach was shown to achieve the lowest drag. The same methods, plus PARSEC, were compared by Masters et al.[25] for shape recovery of a dataset of more than 2000 airfoils. The results varied depending on the error tolerance values used, but considering a range of numbers of design variables, the POD-based approach provided the most efficient design space coverage, while B-splines generally outperformed the FFD approach.

B-spline surface control has been applied extensively and successfully in the authors' research group in two[32] and three[16] dimensions in conjunction with an efficient integrated mesh movement technique. In addition, Gagnon and Zingg[15] have recently developed a novel FFD approach of embedding the surface control points in the FFD volume, which maintains the analytical definition of the geometry, as opposed to the usual approach of embedding the grid nodes.[33–36] The method's robustness has been demonstrated in deforming a sphere into a blended wing-body[37] as well as in the optimization of unconventional aircraft configurations.[38,39] The implementation also features the inclusion of an axial curve to which the FFD volume is attached. The axial curve, whose mathematical definition is decoupled from that of the FFD volume, provides an intuitive way to make large scale changes to the FFD volume.

The question arises as to which geometry control method is preferred for high-fidelity aerodynamic shape optimization, in particular exploratory optimization where substantial shape changes are expected. Previous comparison studies involving the two methods were done in two dimensions.[9,25,31]

The purpose of this paper is to perform a detailed comparison of the two techniques by applying them to a suite of three-dimensional optimization problems in order to determine the limitations and advantages of each. While we compare geometry control through FFD with axial curves with B-spline surface control, geometry parameterization is achieved through B-spline surfaces in both cases.

The comparison study between the two geometry control methods will be conducted by evaluating the methods on the bases of:

- Quality of final shape (objective function value)
- Robustness in dealing with different classes of problems (Euler, Reynolds-averaged Navier-Stokes (RANS); subsonic, transonic; small refinements, large shape changes)
- Ease of use (e.g. problem setup and implementation of constraints)

To provide a basis for comparison, three optimization cases are considered:

- Case 1: Lift-constrained drag minimization, based on the Euler equations giving inviscid flow, of a rectangular wing with a NACA 0012 section, allowing only twist distribution changes, at $C_L = 0.375$ and $M = 0.5$
- Case 2: Lift-constrained drag minimization, based on the RANS equations, of a wing from the Common Research Model (CRM) wing-body configuration of the Fifth Drag Prediction Workshop, allowing section, twist, and angle of attack changes, at $C_L = 0.5$, $C_M \geq -0.17$, $M = 0.85$, and $Re = 5{\times}10^6$
- Case 3: Lift-to-drag ratio maximization, based on the RANS equations, of a blended wing-body (BWB) configuration, allowing section, twist, planform, and angle of attack changes, at $M = 0.80$ and $Re = 62{\times}10^6$

The remainder of the paper is organized as follows: Section II summarizes the algorithms used in the aerodynamic design optimization framework called Jetstream. Section III presents the results obtained for the three optimization problems. Section IV provides a discussion comparing the geometry control methods based on results and experience from the three cases. Section V outlines conclusions and recommended future work.

II. Methodology

A. Integrated Geometry Parameterization, Control, and Mesh Movement

1. B-Spline Curves, Surfaces, and Volumes

A fundamental understanding of B-splines is needed, as they form the building blocks of both geometry control methods studied in this project. A B-spline curve of degree p is defined as the linear combination of basis functions $\mathcal{N}_i^{(p)}$ weighted with control-point coordinates $\{\mathbf{B}_i\}_{i=1}^N$:

$$\mathbf{C}(\xi) = \sum_{i=0}^{N} \mathcal{N}_i^{(p)}(\xi)\mathbf{B}_i \quad a \leq \xi \leq b. \tag{1}$$

The basis functions are functions of computational coordinates ξ and are joined at the knot locations defined by the knot vector

$$T = \{\underbrace{a, ..., a}_{p+1}, \xi_{p+1}, ..., \xi_N, \underbrace{b, ...b}_{p+1}\}. \tag{2}$$

The $p+1$ repeating knots at the ends of the vector ensure that the curve passes through $\mathbf{B}_1$ and $\mathbf{B}_N$. The B-spline basis functions are defined recursively in terms of parameter space and the knot vector as

$$\mathcal{N}_i^{(0)}(\xi) = \begin{cases} 1 & \text{if } \xi_i \leq \xi < \xi_{i+1} \\ 0 & \text{otherwise} \end{cases} \tag{3a}$$

$$\mathcal{N}_i^{(p)}(\xi) = \frac{\xi - \xi_i}{\xi_{i+p} - \xi_i}\mathcal{N}_i^{(p-1)}(\xi) + \frac{\xi_{i+p+1} - \xi}{\xi_{i+p+1} - \xi_{i+1}}\mathcal{N}_{i+1}^{(p-1)}(\xi). \tag{3b}$$

Extending these concepts to multidimensions, a B-spline surface or volume can be defined similarly as a tensor product, with a volume defined as

$$\mathbf{V}(\boldsymbol{\xi}) = \sum_{i=0}^{N_i}\sum_{j=0}^{N_j}\sum_{k=0}^{N_k}\mathcal{N}_i^{(p_i)}(\xi)\mathcal{N}_j^{(p_j)}(\eta)\mathcal{N}_k^{(p_k)}(\zeta)\mathbf{B}_{i,j,k}, \tag{4}$$

where $\boldsymbol{\xi} = (\xi, \eta, \zeta)$ are three-dimensional parametric coordinates.

2. B-Spline Surface Geometry Parameterization and Control

Grid Fitting Procedure

Whether B-spline surface or FFD control is used for the optimization, each block in the multi-block structured mesh is fitted with a cubic B-spline volume with a specified number of control points. Cubic B-spline volumes are typically used, since they accurately and efficiently capture an initial geometry and provide good geometric flexibility.

The fitting procedure for a given block is summarized as follows.[16] The parametric values of the grid nodes are located based on a chord-length parameterization, consistent with the knot vector definition (see below). Next, spatially varying knot vectors are determined, providing a B-spline basis that can be tailored to the geometry to provide a more accurate fit. A chord-length parameterization is used to define the edge knots, which produces a control mesh that is a coarse approximation to the computational mesh. Bilinear knots are used for the internal knots. The control-point coordinates are determined by solving a least-squares problem to best fit the initial volume grid. The results of the fitting are an analytical B-spline surface definition of the geometry and a B-spline control grid that is used for the mesh movement, which is described later. The control mesh is a coarse approximation to the computational mesh. Hyperbolic node distributions are used during mesh generation, and the analytical B-spline volumes describing each block allow for parametric grid refinement that preserves the hyperbolic distribution and produces refined grids of the same "family".

B-spline Surface Control

If B-spline surface control is used, the control points defining the geometry's surface are taken as the design variables. The local support property of B-splines means that the influence of a single control point on the surface is localized. In general, each of these control points can have a degree of freedom in each of the three coordinate directions. To help optimization convergence by minimizing the number of design variables, minimize control point cross-over, and define design variables that are intuitive for aircraft design, certain degrees of freedom can be frozen or constrained into groups. For example, the z-directional freedom can be left free to define sectional design variables, but also constrained to define twist and dihedral design variables. The x-directional freedom is usually constrained to define chord and sweep design variables, and the y-directional freedom constrained to define span design variables. The block face defining a surface is sometimes called a surface patch. Control points around patch interfaces can be constrained to maintain desired levels of continuity, for example, C^1 or C^2 continuity.

A generalized approach for dealing with B-spline surface design variables and constraints called region design variables has been developed[40] and is used for Case 3. The approach was developed to enable the user to optimize a wide range of geometries without the need to implement customized design variable and constraint definitions. It is currently compatible with grid topologies defining the wing in terms of upper and lower surfaces, as is the case for H-H and H-O topologies.

3. Free-Form Deformation Geometry Control

Free-form deformation[28] (FFD) is the second geometry control method to be considered. In traditional aerodynamic design optimization practice, the embedded objects are the surface grid nodes.[33–36] In Jetstream, however, the embedded objects are taken as the B-spline surface control points defining the geometry, and the FFD volume is a cubic B-spline volume.[15] This maintains an analytical definition of the geometry and allows the mesh movement, described later, to be performed in the same way as with B-spline surface control. The FFD volume is created using a geometry generation tool called GENAIR.[41]

Numerically, FFD is executed using two functions. The first is the embedding function and is evaluated only once. The coordinates of the surface control points are mapped from physical space to the parametric space of the FFD volume. This is accomplished using a Newton search algorithm. Referring back to Equation 4, the embedding function determines the ξ, η, ζ parametric coordinates of each embedded surface control point, and these coordinates remain unchanged during the optimization. The second function is the deformation function which algebraically evaluates the new coordinates in physical space of every embedded surface control point once the FFD volume has been deformed. Each time the optimizer adjusts the FFD control-point coordinates $\mathbf{B}_{i,j,k}$, the deformation function given by Equation 4 re-evaluates the surface control-point coordinates $\mathbf{V} = (x, y, z)$.

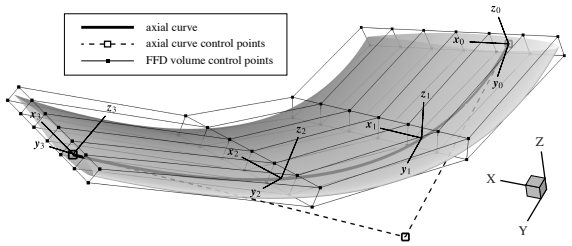

Figure 1: Axial deformation of an FFD volume about a generic wing (Used with permission)[15]

While B-spline surface control couples the design variables with the geometry parameterization, FFD decouples the two, parameterizing deformations rather than the geometry itself. So while the geometric design variables in the surface-based control approach are the surface control points, the geometric design variables in the FFD approach are a set of the FFD volume control points. Gagnon and Zingg[15] describe the deformation process as a two-level approach. The first level involves the control points defining the FFD volume. The second level involves the control points defining the geometry. For all the cases examined in this paper, the FFD volumes are fourth-order in the chordwise and spanwise directions, and second-order in the vertical direction. Having a higher order in the vertical direction would require additional layers of interior FFD control points, rapidly increasing the number of design variables without providing significant benefit for surface control. Interior FFD control points would be of more interest for controlling the interior volume of the geometry, such as for structural design.

Axial Deformation

The FFD approach described above was enhanced by Gagnon and Zingg with the addition of axial deformation capabilities.[15] The concept was introduced by Larazus et al.[42] and is similar in principle to FFD. One or more axial curves are placed within or outside the geometry. The points defining the object are mapped to the nearest point along the curve. The curve is then deformed, and the coordinates of the geometry are re-evaluated based on the mapping to the axial curve.

As an example from Gagnon and Zingg,[15] Figure 1 shows how an axial curve can be used to deform a wing. The axial curve is a B-spline curve given by Equation 1. In this case, it is placed at the quarter-chord, but the leading and trailing edges are also common choices. Each FFD control-point cross-section has its own local orthonormal coordinate system with its origin located on the axial curve and oriented such that the plane of each cross-section remains in line with the free-stream flow direction. The cross-sections remain "attached" to the axial curve as it is deformed through the manipulation of its B-spline control points. As before, the B-spline surface control points are embedded within the FFD volume.

The complete set of design variables are defined as follows:

- Sweep: x-directional translation of axial control points

- Span: y-directional translation of axial control points
- Dihedral: z-directional translation of axial control points
- Twist: rotation or twist of FFD cross-sections about axial curve
- Chord: scaling FFD cross-sections about axial curve
- Section: z-directional translation of FFD control points in the cross-section's local coordinate system

It is worth noting that the particular cases in this paper focus more on the FFD design variable capabilities, i.e. twist, chord, and sectional changes, and do not exploit the full capabilities of the axial curve.[15,38]

4. Linear-Elasticity Mesh Movement

The method employed in Jetstream to update the computational mesh once the geometry has been modified is based on a linear-elasticity model.[43] The model is applied to the control mesh rather than the computational mesh, making the mesh movement much cheaper to compute while still maintaining high mesh quality.[16] The algorithm can be performed in increments to improve mesh quality for large shape changes. Since the original mesh fitting provides the parametric values of the grid nodes, algebraic recomputation of their coordinates in physical space is quick to perform.

B. Flow Solver

The flow solver in Jetstream is a three-dimensional multi-block structured finite-difference solver. The parallel implicit solver uses a Newton-Krylov-Schur method and is capable of solving the Euler or Reynolds-averaged Navier-Stokes (RANS) equations.[44,45] Spatial discretization of the governing equations is performed using second-order summation-by-parts operators. Boundary and block interface conditions are enforced weakly through simultaneous approximation terms, which allow C^1 discontinuities in mesh lines at block interfaces. Deep convergence is efficiently achieved using an inexact-Newton phase, while globalization is provided by an approximate-Newton start-up phase. The resulting large, sparse linear system is solved using the flexible generalized minimal residual method with an approximate-Schur parallel preconditioner. The RANS equations are closed using the Spalart-Allmaras one-equation turbulence model. A scalar artificial dissipation scheme[46,47] is used for the cases in this thesis, but matrix dissipation[48] can also be used.

C. Gradient Evaluation and Optimization Algorithm

The general optimization problem can be posed as follows:

$$\min \ \mathcal{J}(\mathbf{v}, \mathbf{q}, \mathbf{b}^{(m)}) \tag{5a}$$

$$\text{w.r.t. } \mathbf{v} \tag{5b}$$

$$\text{s.t. } \boldsymbol{\mathcal{M}}^{(i)}(\mathbf{A}^{(i)}(\mathbf{v}), \mathbf{b}^{(i)}, \mathbf{b}^{(i-1)}) = \boldsymbol{\mathcal{R}}(\mathbf{v}, \mathbf{q}, \mathbf{b}^{(m)}) = 0, \ i = 1, 2, ..., m \tag{5c}$$

where $\mathcal{J}$ is the objective function, $\mathbf{v}$ are the design variables, $\mathbf{b}^{(i)}$ are the volume control-point coordinates at mesh movement increment i, m is the total number of mesh movement increments, $\boldsymbol{\mathcal{M}}^{(i)}$ are the mesh residuals, $\boldsymbol{\mathcal{R}}$ are the flow residuals, $\mathbf{q}$ are the flow variables, and $\mathbf{A}^{(i)}$ are the displaced surface control-point coordinates. The design variables $\mathbf{v}$ are either a subset of $\mathbf{b}^{(m)}$, if using B-spline surface geometry control, or the FFD control points, if using FFD geometry control, and may also include angle of attack. There can be additional linear and nonlinear equality and inequality constraints.

1. Gradient Evaluation

Gradients are calculated using the discrete-adjoint method at a cost virtually independent of the number of design variables. While it has been shown that gradient-based multistart or hybrid algorithms can be used for multimodal problems,[49] this approach is not taken here. Therefore, the minima achieved are local minima, and may or may not be global minima. For optimality, the Karush-Kuhn-Tucker (KKT) conditions must be satisfied.[50] Once the mesh movement and flow solution have been computed, the resulting flow and mesh adjoint equations must be solved. The flow Jacobian matrix is formed by linearizing its components, including the viscous and inviscid fluxes, the artificial dissipation, the turbulence model, and the boundary conditions. The flow adjoint system is solved using a modified, flexible version of GCROT,[51–53] and the mesh adjoint system is solved using a preconditioned conjugate-gradient method.

2. SNOPT

Once the gradients are computed, they are passed to SNOPT (Sparse Nonlinear OPTimizer),[54] a gradient-based optimization algorithm. It can handle both linear and nonlinear constraints, satisfying linear constraints exactly. SNOPT applies a sparse sequential quadratic programming algorithm that approximates the Hessian using a limited-memory quasi-Newton method.

Table 1: Case 1 - Grid size, off-wall, leading-edge, and trailing-edge spacing, and functional values for initial rectangular planar wing grids

Grid	Nodes	Spacing (c)	C_D	Span Efficiency
Coarse	1,361,976	3×10^{-3}	0.00731	1.000
Medium	10,895,808	1.5×10^{-3}	0.00742	0.986
Fine	36,773,352	1×10^{-3}	0.00747	0.979
Superfine	87,166,464	7.5×10^{-4}	0.00749	0.977

III. Results

A. Case 1: Twist Optimization of a Rectangular Wing in Inviscid Subsonic Flow

1. Optimization Problem

The optimization problem is the drag minimization of a rectangular wing with zero-thickness trailing-edge NACA 0012 sections in inviscid, subsonic flow.[55] The freestream Mach number is 0.5. The design variables are the twist of sections along the span about the trailing edge. Twist is performed by allowing the z-coordinates of the B-spline surface or FFD control points to vary under linear constraints, linearly shearing the sections. The twist at the root section is allowed to vary, while the angle of attack is fixed. The target lift coefficient is 0.375. The twist distribution should produce a lift distribution close to elliptical and an efficiency factor close to unity. The problem can be summarized as

$$\begin{aligned} &\text{minimize } C_D \\ &\text{w.r.t. } \gamma(y) \\ &\text{subject to } C_L = 0.375 \end{aligned}$$

where C_D and C_L are the drag and lift coefficients, respectively, and $\gamma(y)$ is the twist distribution along the span. The initial geometry is a rectangular, planar wing with NACA 0012 sections. The trailing edge is sharp. The semi-span is $3.06c$, with the last 0.06 leading to a pinched tip.

2. Grid

An H-H-topology grid is used for this case. To establish grid convergence, the optimization level grid is refined by a factor of 2, 3, and 4 in each direction, giving the grid family with parameters shown in terms of chord units in Table 1. The locations of the new nodes added during refinement preserve the hyperbolic nodal distribution.

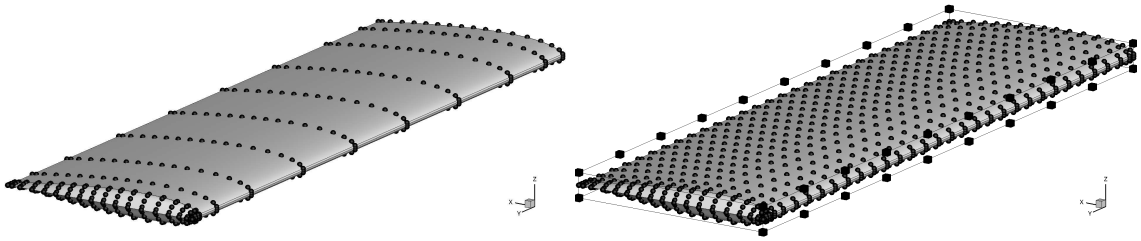

(a) Initial B-spline optimization setup (b) Initial FFD optimization setup

Figure 2: Case 1 - Initial 10 twist design variables for B-spline surface (spheres) and FFD (cubes) control

Drag coefficient and span efficiency factor at $C_L = 0.375$ are reported in in Table 1 for the different grid levels. The medium and superfine grids, which differ in grid size by a factor of 2 in each direction, give C_D values within 1 drag count of each other. The span efficiency factor of the initial geometry is unity on the coarse mesh, but the refinement study shows there is in fact room for improvement. The superfine mesh is chosen for refined analysis of the optimized geometries.

3. Geometry Control Setup

The upper and lower wing surfaces are each parameterized by two surface patches. For the B-spline surface optimizations, the twist for the spanwise stations on the tip patches is constrained to be a linear extrapolation of the twist between the two adjacent stations on the inboard patches. This prevents the optimizer from exploiting the surface control point clustering at the tip to create a non-planar feature. This is not necessary for the FFD optimizations since the FFD spanwise stations are uniformly spaced along the span. This highlights one of the advantages of FFD's decoupling of the design variables from the surface definition. In some cases, a large number of surface control points may be needed to accurately define a certain geometric feature - in this case, the wing tip cap - but a high degree of geometric flexibility in this region may not be desired. With B-spline surface control, this necessitates additional constraints to be implemented, while with FFD, design variables can be clustered to strategically give fine control only where needed.

For all optimizations, 19 chordwise surface control points per surface are used to parameterize the geometry. For the FFD optimizations, 31 spanwise surface control points are used on the inboard patches. Five spanwise surface control points are used for the tip patches in all cases to maintain a consistent tip cap geometry. Fewer surface control points were used for the tip patches in comparison to the inboard patches due to their relative difference in size. In addition, using too many surface control points at the tip can increase the risk of control point crossover. For both geometry control techniques, the number of twist design variables is varied up to a maximum of ten; the initial design variables for both ten design variable cases are displayed in Figure 2.

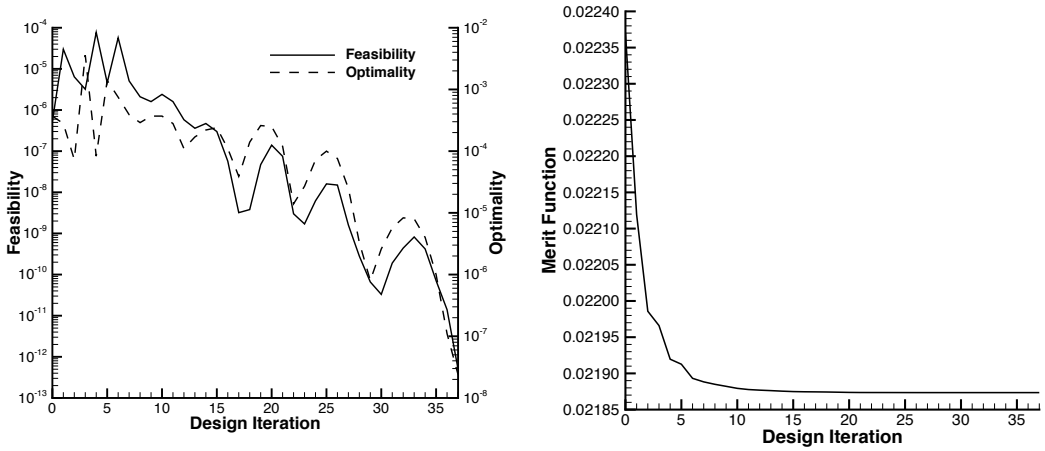

(a) Feasibility and optimality histories

(b) Merit function history

Figure 3: Case 1 - SNOPT convergence history for the optimization with 10 B-spline surface design variables

4. Optimization Results

The optimizations are conducted on the coarse mesh with different numbers of B-spline surface and FFD design variables. All of the optimizations are successful, reaching feasibility and optimality tolerances of 1×10^{-6} and 1×10^{-7}, respectively. Feasibility is the largest nonlinear constraint violation, optimality is a measure of how well the KKT conditions are satisfied, and merit function is the objective function plus a penalty term for nonlinear constraint violations. For example, the feasibility, optimality, and merit function histories for the optimization with 10 B-spline surface design variables are displayed in Figure 3. In this case, the merit function tracks with $C_D A$, where A is the wing area in nondimensional units based on the chord length. A similar number of optimization iterations is needed with 10 FFD design variables. The optimized geometries are re-analyzed on the superfine mesh, with the angle of attack adjusted in each case to satisfy the C_L constraint of 0.375. The drag coefficients and span efficiency factors of the initial and optimized geometries are plotted in Figure 4. All of the optimized span efficiencies are very close to unity. For a given number of design variables, the difference in drag between the B-spline surface and FFD optimized geometries is insignificant, only about 0.1 counts. As expected, the spanwise lift distributions are close to elliptical. For example, the lift distributions obtained with 10 design variables are compared to the initial and elliptical distributions in Figure 5. The only noticeable deviation from an elliptical distribution occurs at the tip. The load distributions from the B-spline surface and FFD optimizations are indistinguishable. The two control methods perform equally well in minimizing drag for this case.

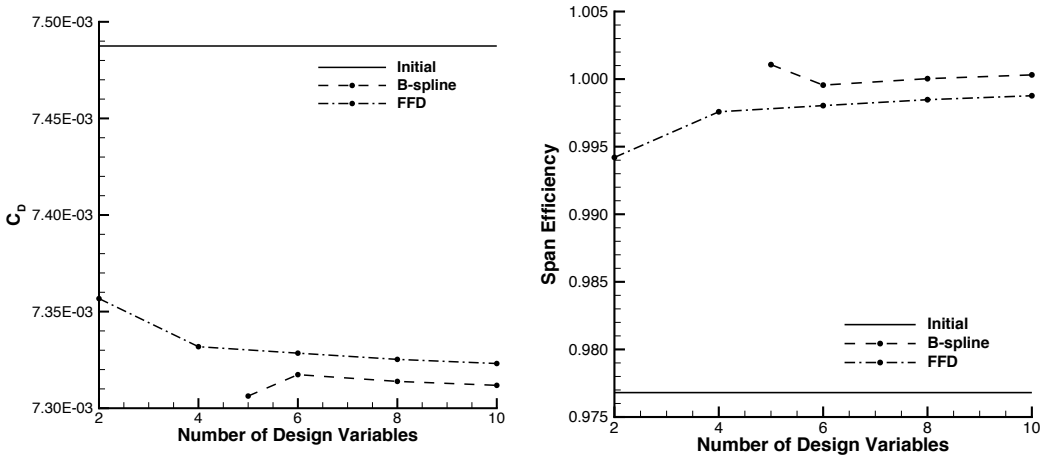

(a) Drag coefficient

(b) Span efficiency

Figure 4: Case 1 - Initial and optimized drag coefficient and span efficiency evaluated on the superfine mesh for different numbers of design variables

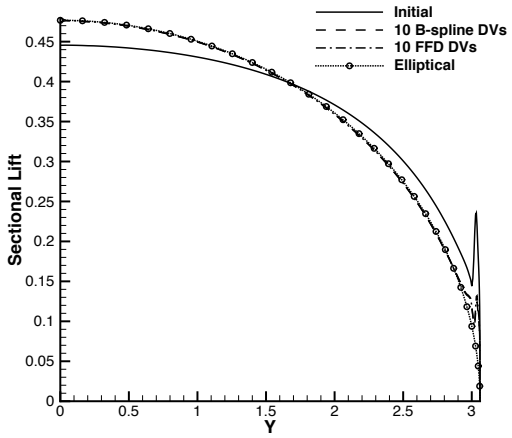

Figure 5: Case 1 - Lift distributions from the 10 design variable optimizations, analyzed on the superfine mesh, compared to initial and elliptical distributions

B. Case 2: Twist and Section Optimization of CRM Wing in Turbulent Transonic Flow

1. Optimization Problem

The second optimization problem is the drag minimization of the Common Research Model (CRM) wing at a Mach number of 0.85 and a Reynolds number of 5 million, where the reference length is the mean aerodynamic chord (MAC).[40] The lift and pitching-moment coefficients are constrained at $C_L = 0.5$ and $C_M \geq -0.17$, respectively. The moment centre, taken from the wing-body configuration and scaled by the MAC, is taken at (1.2077, 0, 0.007669). Coefficients are calculated using the projected area of 3.407014 squared reference units. The design variables are the z-coordinates of the B-spline surface or FFD control points, as well as angle of attack, which is initially set to 2.2 degrees. The trailing-edge surface control points are fixed to permit arbitrary wing twist about the trailing edge, except at the root, where the leading-edge surface control point is also fixed. The volume must be greater than or equal to the initial volume of 0.2617

Table 2: Case 2 - Grid parameters for CRM wing grid study

Grid	Nodes	Off-wall Spacing (MAC)	y^+
Coarse	925,888	1.5×10^{-6}	0.33
Fine	7,407,104	8.1×10^{-7}	0.17
Superfine	58,456,064	3.9×10^{-7}	0.081

cubed reference units, and the sectional thickness t must remain greater than or equal to 25% of the initial thickness t_{baseline}. This problem formulation leads to a wing that is excessively thin in places and therefore not structurally practical, but the high degree of geometric freedom permitted makes it a good test of the optimization methodology. The problem can be summarized as follows:

$$\begin{aligned} &\text{minimize } C_D \\ &\text{w.r.t. } z, \alpha \\ &\text{subject to } C_L = 0.500 \\ &\qquad C_M \geq -0.17 \\ &\qquad V \geq V_{\text{baseline}} \\ &\qquad t \geq 0.25 \times t_{\text{baseline}}. \end{aligned}$$

2. Initial Geometry

The initial geometry is the wing of the Common Research Model wing-body configuration from the Fifth Drag Prediction Workshop,[56] which has a blunt trailing edge. The wing geometry was obtained by removing the fuselage, translating the leading-edge root to the origin, and scaling the geometry by the MAC of 275.8 inches.[40]

3. Grid

An O-O-topology grid was used for this case. The O-O-topology is better suited for the blunt trailing edge than the H-H-topology and also provides a more efficient nodal distribution, enabling equivalent numerical accuracy with significantly fewer grid nodes in comparison to the H-H grid topology used in the first optimization problem. The coarse grid was refined by factors of 2 and 4 in each direction using parameter refinement to produce fine and superfine grids, and the grid family is described in Table 2. Table 3 provides the drag and moment coefficients calculated from the refinement study for the baseline geometry, with the angle of attack adjusted to give a lift coefficient of 0.5 in each case.

Table 3: Case 2 - Results for CRM wing optimization

	Optimization Mesh		Fine Mesh		Superfine Mesh	
	C_D (counts)	C_M	C_D (counts)	C_M	C_D (counts)	C_M
Baseline	221.6	-0.174	201.5	-0.175	199.1	-0.175
B-spline surface control	196.9	-0.170	185.2	-0.170	185.6	-0.170
FFD control	199.0	-0.170	186.8	-0.171	185.4	-0.171

4. Geometry Control Setup

The O-O grid topology gives leading- and trailing-edge patches which are not compatible with the required top and bottom surface definitions of the region design variable approach,[40] described in Section 2, for generalizing the treatment of B-spline surface control. As a result, thickness and patch interface continuity constraints must be developed for this specific topology. On the other hand, the FFD formulation does not depend on the topology of the underlying geometry, so no special treatment is needed for the thickness constraints applied to the FFD control points. The thickness constraints are implemented in a more general form that works for arbitrary grid topologies. Due to the two-level nature of the FFD control, however, the thickness constraints are not as precisely enforced as with B-spline surface control. Nonlinear patch interface continuity constraints are not implemented for FFD since the larger FFD control point spacing relative to the surface control point spacing at the interface is expected to give negligible discontinuities.

However, the requirements of fixed trailing-edge and leading-edge root control points are more easily treated using B-spline surface control. With B-spline surface control, this simply involves giving these control points zero freedom. With FFD, one does not have direct control of the surface control points, so achieving the same result with FFD is more involved. In general, an embedded point's position is affected by the number of FFD control points in each direction equal to the order of the B-spline volume in that direction. So for the FFD volumes used for this case, which are fourth-, fourth-, and second-order in the chordwise, spanwise, and vertical directions respectively, a general constraint fixing a single embedded point requires constraining $4 \times 4 \times 2 = 32$ FFD control points. Such constraints are inherently not as localized as the B-spline surface treatment and could limit geometric freedom to a greater extent. In the case of the trailing-edge, the number of FFD points which are affected by the constraint can be reduced by placing the trailing edge of the FFD volume in line with the trailing-edge surface control points, but this cannot be applied practically as a general approach for constraining arbitrary surface points. The linear equality constraint equation implemented to achieve this comes directly from Equation 4, restated here specifically for z, the z-coordinate of the surface control point of interest, as a function of B_z, the z-coordinates of the

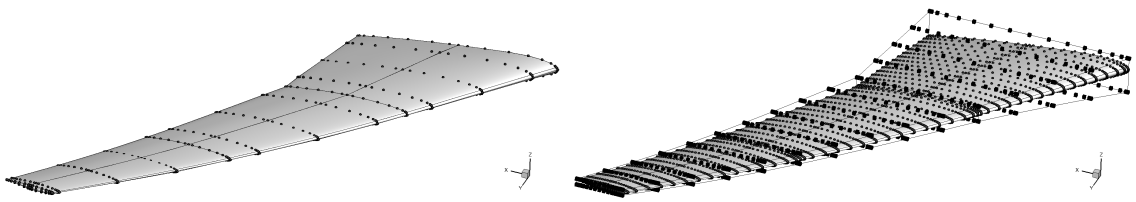

(a) Initial B-spline optimization setup (b) Initial FFD optimization setup

Figure 6: Case 2 - Initial design variables for B-spline surface (spheres) and FFD (cubes) control

FFD control points:

$$z(\boldsymbol{\xi}) = \sum_{i=0}^{N_i} \sum_{j=0}^{N_j} \sum_{k=0}^{N_k} \mathcal{N}_i^{(p_i)}(\xi) \mathcal{N}_j^{(p_j)}(\eta) \mathcal{N}_k^{(p_k)}(\zeta) B_{z_{i,j,k}}. \tag{6}$$

5. Results

For B-spline surface geometry control, there are a total of 15 spanwise design sections, and each section is controlled by 35 surface control points. For FFD geometry control, two FFD volumes are joined at the wing crank and give 15 spanwise design sections, each controlled by 17 chordwise FFD control points on the top and bottom, giving a similar number of design variables to the B-spline surface control setup. The FFD points are clustered towards the leading and trailing edges according to a cosine distribution. The design variables for both cases are displayed in Figure 6.

To verify that the B-spline accurately captures the geometry, flow solutions are computed on the baseline grid without fitting and on the fitted grid with sections controlled by 35 surface control points. Percentage differences of 0.2% for C_L and 0.1% for C_D are obtained. This verifies that 35 surface control points are adequate to obtain a good fit to the original geometry.

Optimizations are conducted using both geometry control methods on the coarse grid. The results of the optimizations are summarized in Table 3, which provides the C_D and C_M computed on the optimization, fine, and superfine mesh levels, with the angle of attack adjusted to give $C_L = 0.5$. On the coarse mesh, B-spline surface control gives lower drag than FFD by about 2 counts. The drag differential essentially disappears, however, when the final geometries are evaluated on the superfine mesh.

Sectional pressure plots evaluated on the superfine mesh and airfoil sections are plotted in Figure 7. The B-spline surface and FFD pressure plots are quite similar, especially for the first five spanwise stations. The difference at the tip could be due to slight multimodality or design space flatness. The pressure recovery in the tip region appears somewhat smoother with the B-spline surface. On the coarse mesh used for optimization, the shocks are eliminated, but weak shocks reappear on the finer mesh used for subsequent analysis. Both control methods have thinned out the sections along most of the wing to reduce wave drag, while thickening the root region significantly due to the volume constraint. A high degree of sectional control is demonstrated

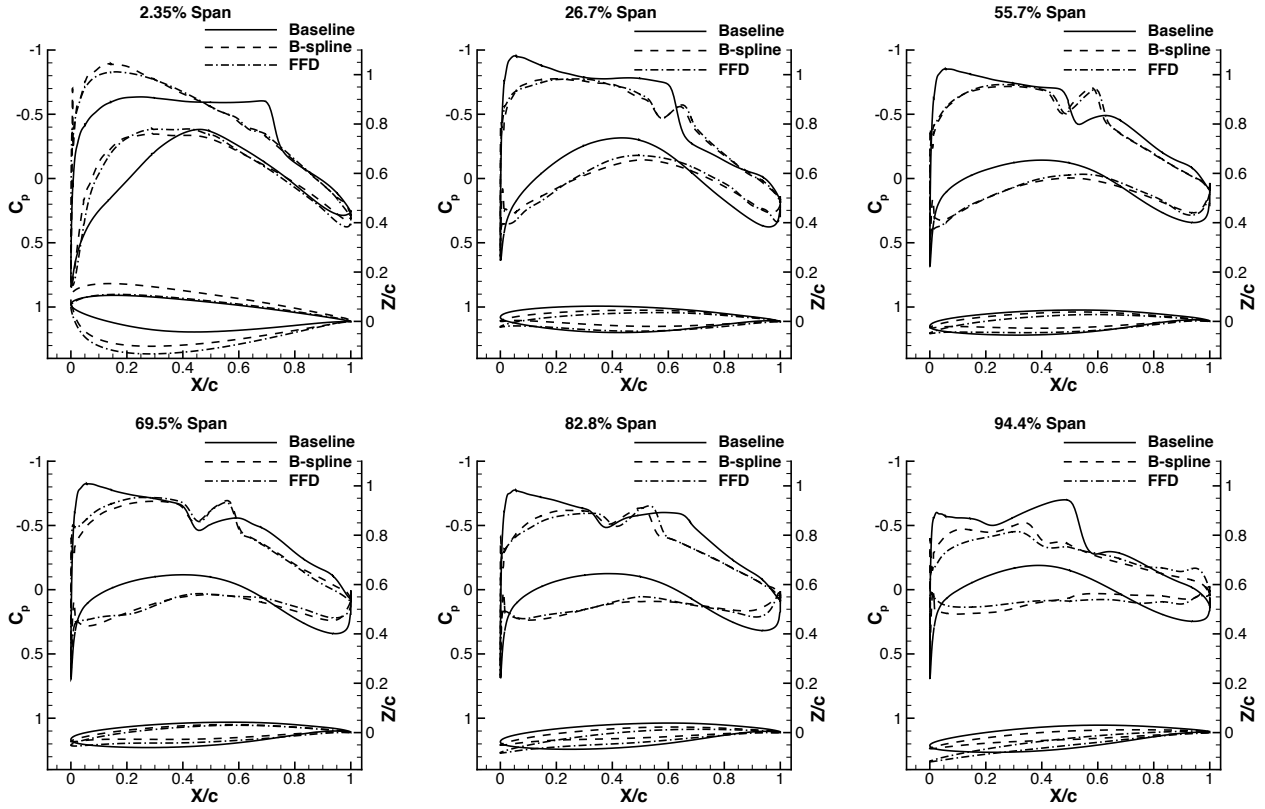

Figure 7: Case 2 - Sectional pressure plots and sections for baseline and optimized CRM wings computed on superfine mesh

by both parameterizations with the highly cambered leading edges, for example at 26.7% span. Despite the leading-edge root control point being fixed by both cases, the wing from the B-spline surface optimized appears to have higher twist overall, and the final angle of attack is lower.

Figure 8 shows the convergence history of SNOPT for the two optimizations on the coarse mesh. The feasibility and optimality tolerances are both set at 1×10^{-6}. Optimality is reduced by about two orders of magnitude with respect to its highest value in each case. The differences in initial optimality as well as the convergence rate between B-spline surface and FFD control may be due to design variable scaling. Greater reduction in optimality for the B-spline case is possible with further optimization; however the merit function plot, which tracks with C_DA, shows that most of the drag reduction has already been achieved. The merit function for the FFD optimization is also flattening out, but is not quite as flat. The optimization exited, however, since the optimality tolerance was reached. The FFD optimization was repeated with a lower optimality tolerance, but this affected the convergence path taken by SNOPT and led to poorer convergence and an earlier optimization termination. With the exception of this attempt to lower the optimality tolerance, standard settings were consistently used for SNOPT to ensure generality of results and conclusions. Finally, it is important to recall that the better performance seen from the geometry obtained using B-spline surface control largely disappears when the analysis is performed on the finer mesh. The additional geometric con-

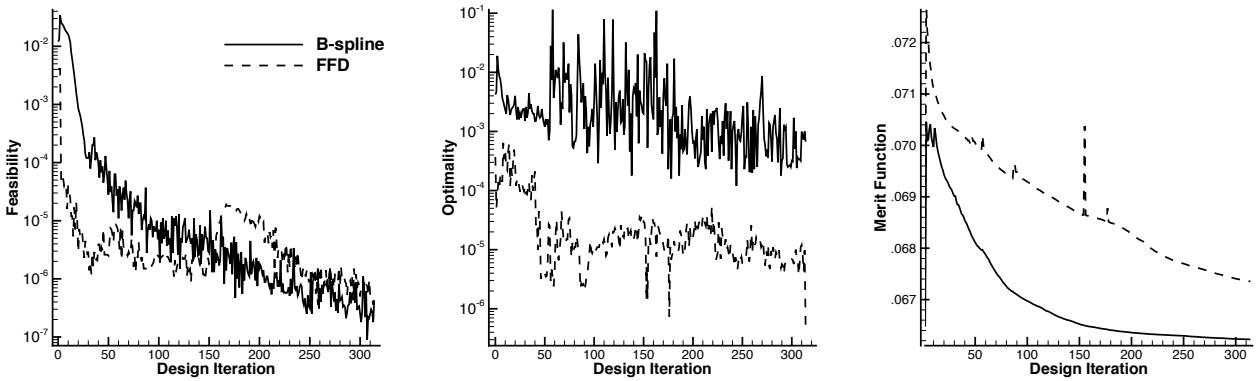

Figure 8: Case 2 - SNOPT convergence for coarse mesh optimizations of the CRM wing

trol afforded by B-spline surface control seems to only provide additional improvement of the same order of truncation error.

C. Case 3: Exploratory Optimization of a Blended Wing-Body in Turbulent Transonic Flow

1. Optimization Problem

The optimization problem is the maximization of the lift-to-drag ratio of a blended wing-body (BWB) sized for 100 passengers at a freestream Mach number of 0.8 and a Reynolds number of 62 million, corresponding to a cruise altitude of 40,000 ft., based on the work of Reist and Zingg.[57] In contrast to the two previous optimization problems, the objective function here minimizes $-\frac{L}{D}$, and no lift or moment constraints are enforced. In the context of the work of Reist and Zingg,[57] this type of optimization was used to find a lifting-fuselage configuration that is significantly different from the classical BWB design; it was followed up with a refined optimization incorporating weight estimates and lift and trim constraints. The baseline geometry is a classically shaped BWB based on symmetric airfoil sections. The initial angle of attack is zero, so the initial lift-to-drag ratio is zero. Our focus is on the difference between the geometries optimized using the two geometry control methods, rather than a comparison with the classically shaped BWB; such a comparison can be found in Reist and Zingg.[57] The design variables include the z-coordinates of the B-spline surface or FFD control points, twist about the leading edge, chord, as well as the angle of attack. In addition, the spans of the body and wing can vary, but the total span of 118 ft. and leading-edge sweep are kept constant. To allow this optimization to be exploratory in nature, few constraints are imposed. The body and wing leading edges and wing trailing edges must remain straight. The body volume and projected area are constrained as $V_{\text{body}} \geq 10,000$ ft^3 and $A_{\text{body}} \geq 1540$ ft^2, respectively, and the wing volume is constrained as $V_{\text{body}} \geq 4500$ gal. The design variable and constraint bounds are summarized in Table 4. In addition, linear twist on the body and wing is enforced. Linear taper is enforced on the wing, but the body

Table 4: Case 3 - Design variable and constraint bounds for BWB optimizations

Design Variable	Lower Bound	Upper Bound
Twist	-10°	+10°
Chord	-50%	+50%
Section	-75%	+100%
Body/wing span	-75%	+75%
Angle of attack	-3°	+3°
Constraint	**Lower Bound**	**Upper Bound**
Taper ratio	0.1	1.0
Section thickness	-75%	+100%
Body projected area	1540 ft^2	N/A
Body volume	10,000 ft^3	N/A
Wing volume	4500 gal	N/A

Table 5: Case 3 - Grid parameters for BWB grid study

Grid	Nodes	Off-wall Spacing (MAC)	y^+
Coarse	1,225,728	1.3×10^{-6}	2.13
Fine	9,805,824	5.7×10^{-7}	0.94

can deviate from linear taper by a distance of up to 25% of the initial body semi-span. The initial geometry is scaled by the MAC of 40.6 ft.

2. Grid

An H-O-topology grid is used for this case. The optimization grid is refined by a factor of two in each direction, giving the grid parameters shown in Table 5. Optimizations are conducted on the coarse grid, and the fine grid is used to analyze the initial and final geometries.

3. Geometry Control Setup

The B-spline surface controlled optimizations are conducted using the region design variable approach;[40] hence no additional setup was required. The body and wing are defined as separate regions. The following constraints had to be added to the FFD code: taper ratio, projected area and volume for the desired regions, fixed sweep for varying region span, and nonlinear taper deviation. These were implemented in a consistent way to the B-spline surface approach with no additional complexity. The FFD control points are clustered in the chordwise direction according to a cosine distribution. While linear constraints with B-spline surface control are used to ensure the geometry surface intersects the symmetry plane at a perpendicular angle, this is not enforced with FFD. Although there are wide variety of design parameters in this problem, SNOPT makes no distinction between the different types of parameters; it just sees a numerical array of design variables.

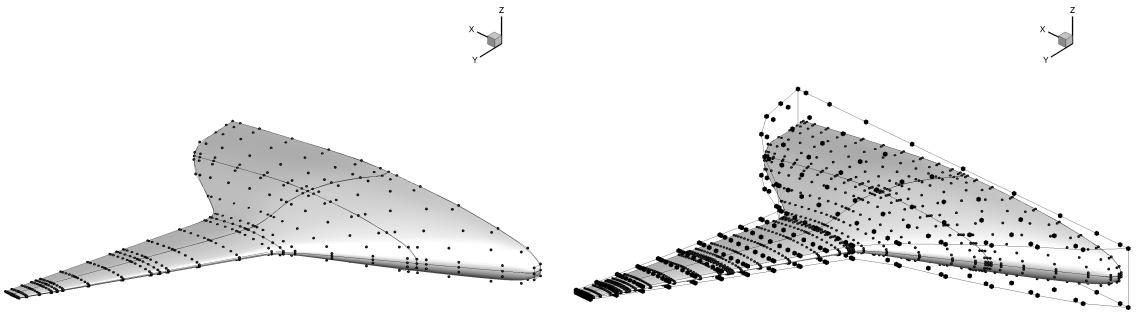

(a) Initial B-spline optimization setup

(b) Initial FFD optimization setup

Figure 9: Case 3 - Initial design variables for B-spline surface (spheres) and FFD (cubes) control

Table 6: Case 3 - Results for BWB optimization

	Coarse Mesh			Fine Mesh		
	C_L	C_D (counts)	$\frac{C_L}{C_D}$	C_L	C_D (counts)	$\frac{C_L}{C_D}$
Baseline	0.000	96.6	0.00	0.000	84.1	0.00
B-spline surface control	0.298	124.2	23.96	0.306	123.9	24.67
FFD control	0.299	125.5	23.83	0.305	125.2	24.40

Design variable scaling can be applied to particular design variables to adjust their relative gradients and attempt to emphasize particular design changes. This was not done, however, to maintain the generality of the optimization methodology, and since the design variables are already defined to be of the same orders of magnitude between the two methods, providing a fair comparison.

For B-spline surface control, the geometry is controlled using 11 chordwise by 17 spanwise surface control points, while for FFD control, 11 by 17 FFD control points are used. The design variables for both cases are displayed in Figure 9.

4. Results

Optimizations are conducted on the coarse grid, and the functionals for the initial and optimized geometries evaluated on the coarse and fine grids are displayed in Table 6. The angle of attack was maintained at the respective design value for the fine mesh analyses: 0.281° for B-spline surface and 2.534° for FFD. While the change in C_D is large, over 12 counts, between the different meshes for the initial geometry, the change is 0.3 counts for the optimized geometries. It has been found that on a given mesh, a blunter leading edge produces stronger pressure gradients and can lead to higher spurious drag and greater grid dependency.[58] This is consistent with what is observed in this case; as shown in Figure 10, the leading edges along the span of the initial geometry are more blunt than those along the span of the optimized geometries, giving lower grid dependency for the optimized geometries. Hence, the fine-mesh evaluation was deemed sufficiently

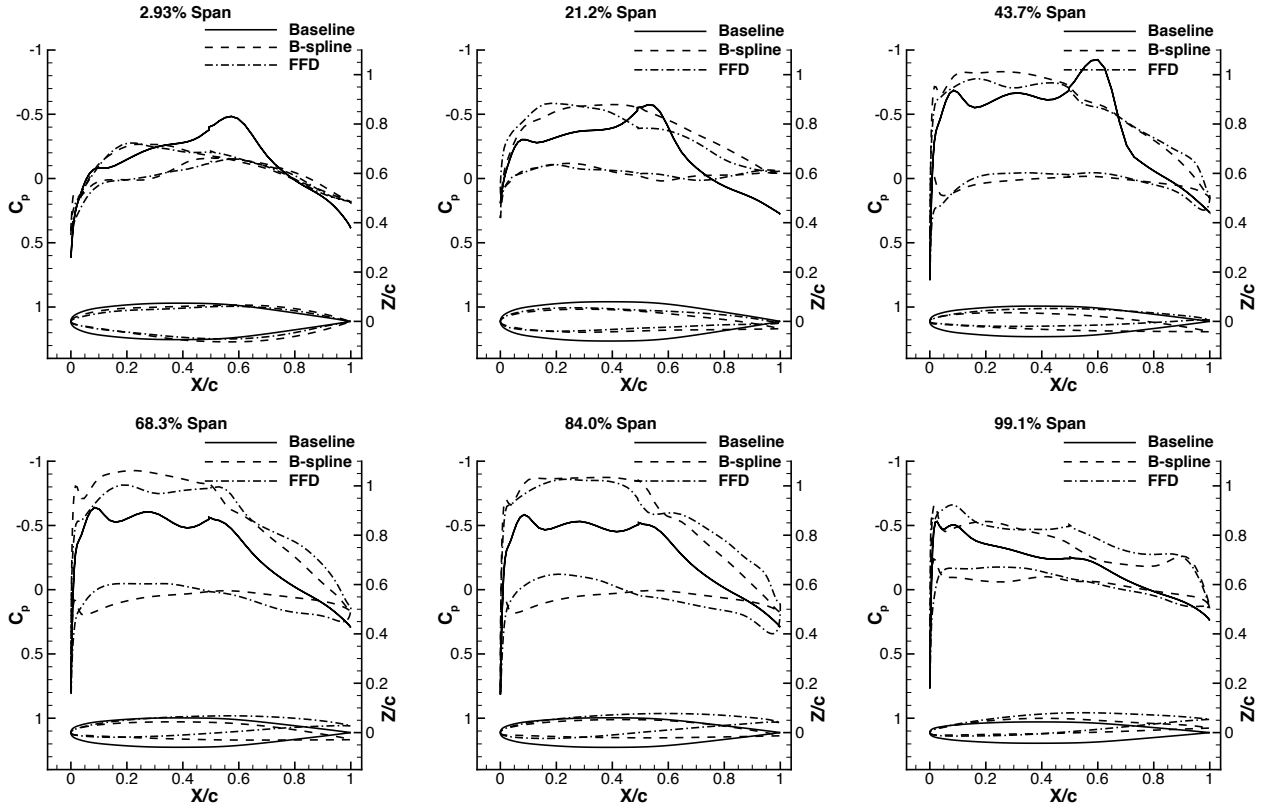

Figure 10: Case 3 - Sectional pressure plots and sections for baseline and optimized BWBs computed on fine mesh

accurate for the purposes of the comparison study between the geometry control methods. The C_L, C_D, and $\frac{C_L}{C_D}$ ratios are all very comparable between the optimized geometries. The $\frac{C_L}{C_D}$ ratio from B-spline surface control is about 1% higher than that which is achieved using FFD, when analyzed on the fine mesh.

The upper-surface pressure contours, evaluated on the fine mesh, for the initial and optimized geometries are compared in Figure 11. The planform of the BWB changes significantly from the traditional "home plate" shape. The root chord increases significantly and a sharper body trailing-edge line is formed. The span of the wing increases, decreasing the span of the body and pushing the wing root more forward. The shock that is present on the initial geometry near the wing-body junction is removed in both cases. While the two optimized pressure contours are comparable, the isobars on the B-spline surface controlled geometry are noticeably smoother than on the FFD geometry, which may be indicative of superior sectional control provided by the B-spline surface control.

Sectional pressure distributions evaluated on the fine mesh and airfoil sections are displayed at select spanwise stations for the initial and optimized geometries in Figure 10. The 2.93% span distributions are quite similar, and the 43.7% span distributions are comparable, but the remaining distributions are quite different. The geometry resulting from the FFD geometry control displays significant outboard washout, which explains the higher angle of attack needed to achieve a similar lift coefficient. In general, the B-spline

surface controlled geometry has smoother pressure distributions. It is not clear why two different geometries are produced in this case. It is possible these are two different local minima with similar performance.

The SNOPT convergence history is displayed in Figure 12. The absence of data at the start of the feasibility plots is due to the feasibility being zero at this stage of the optimizations. The FFD optimality begins and remains lower than that of the B-spline surface optimization, likely due to differences in mathematical definitions of their design variables. Interestingly, the merit functions, $-\frac{C_L}{C_D}$ in this case, begin to converge at a near identical rate. To conclude, similar $\frac{C_L}{C_D}$ values are achieved with the geometry control methods, with B-spline surface control performing slightly better.

IV. Discussion

Based on the results and experience derived from the three optimization cases, comparisons can be made between the two geometry control methods in terms of their ability to improve designs and ease of setup for aerodynamic shape optimization.

A. Performance of Optimized Geometry

The CRM wing and BWB cases showed B-spline surface control performing marginally better than FFD at optimizing the objective functions in question and providing smoother pressure distributions on the geometries. While the differences were minor, especially when the optimized designs were analyzed on finer meshes, these cases provide evidence that B-spline surface control offers superior shape control. When a given geometry is analyzed, the flow solver has no concept of the B-spline surface or FFD control points. Rather, it is the surface mesh that defines the geometry under analysis. The B-spline surface control points provide a close approximation of the surface mesh. In fact, in some locations on the geometry, such as the leading and trailing edges, there is often a one-to-one mapping where a surface control point directly controls a corresponding surface node.

A disadvantage of the FFD implementation is that the FFD control points do not follow the curvature of the geometry nearly as well as the surface control points. As a result, the geometry surface is less sensitive to the FFD control points, particularly where the space between the surface and FFD control points is larger, so the optimizer must compensate by larger changes in the design variables. For these reasons, B-spline surface control provides better local control of the geometry than the FFD approach, leading to lower drag in the CRM case and higher $\frac{C_L}{C_D}$ in the BWB case.

B. Geometry Control Setup

In addition to their ability to optimize objective functions, the geometry control methods can also be compared on the basis of their usability for shape optimization setup. It was found that both geometry control methods have their advantages and disadvantages.

One advantage for B-spline surface control comes from the fact that it offers direct control over some key geometry points, such as at the leading and trailing edges, while for FFD, there is no such one-to-one mapping. As a result, certain conceptually simple constraints, such as fixing the leading-edge root and trailing edge control points in the CRM wing case, are trivial for B-spline surface control, but more involved for FFD.

Not only is the FFD approach for achieving these constraints more complicated to implement, but the constraints themselves are also much less localized. Recall that for an FFD volume of orders 4, 4, and 2 in each coordinate direction, 32 FFD control points must be constrained to fix a single embedded surface point in space. Such constraints can make optimization convergence more difficult with FFD.

However, the fact that FFD decouples the geometric design variables from the surface definition provides several key advantages. First, the level of control offered by the FFD setup can be set completely independently of the complexity of the underlying geometry. One implication of this is that the user does not have to provide more control than desired. An example of this was seen with the twist optimization. To resolve the curvature of the wing tip, surface control points had to be clustered toward the tip, offering more control than needed in this region. A linear constraint was implemented to limit the flexibility of the design at the tip under B-spline surface control, requiring more setup work and restricting the design in a non-ideal way. With FFD, no such constraint was necessary, since the spanwise spacing of the FFD control points was much larger, and was definable independent of the wing-tip curvature. Note that if tight spanwise clustering of the FFD control was in fact desired, this would have been simple to set up as well. Another implication of the level control of FFD not being tied to the complexity of the geometry is that design variable and constraint implementation can be significantly simplified. As a conceptual example for this, one can imagine the amount of work necessary to define a simple elongation design variable along a coordinate direction using B-spline surface control for a very complex geometry. Many surface control points would be needed to resolve the geometry, bringing with it many degrees of freedom that would have to be constrained into a single design variable. The much simpler method would be to just create a rectangular FFD volume of order 2x2x2 in each direction around the geometry and define the elongation design variable using only the 8 FFD control points needed to define the volume. The conceptual simplicity of controlling the FFD volume using an axial curve defined by just a few axial control points also highlights this point.

The decoupled nature of FFD from the surface also makes it easier to modify only certain parts of the geometry, while leaving the rest unchanged, for example modifying only the leading edge of a wing. To achieve this with B-spline surface control, care must be taken to keep track of surface patch and control point indices while implementing new code to define localized design variables and constraints. Although this is straightforward on simple geometries, it can be tedious on more complex geometries. On the other hand, an FFD volume can be created only surrounding the region of interest to provide localized control in a much more general and efficient way.

FFD's decoupling of design variables from the surface also makes constraint and design variable implementation more intuitive and general, irrespective of the computation grid topology used. This was seen with the CRM wing case, where standard FFD thickness constraints were used but new B-spline surface thickness constraints had to be implemented due to the fact that an O-O grid topology was being used instead of the usual H-H topology. The regularity of FFD volumes allows a general set of constraints and design variables to be implemented on the FFD volume. On the other hand, since the patch and surface control point indexing and interdependence depends on the grid topology being used, design variables and constraints tend to be hardcoded depending on the grid topology. Key implications of this difference is that FFD can more readily be used to deal with complex geometries yielding complex grid topologies, such as unconventional aircraft configurations,[15] as well as more easily be implemented with a multistart algorithm.[49]

A final advantage of FFD coming from the decoupling of the design variables from the surface parameterization is that FFD lends itself more easily to progressive (uniform) and adaptive (strategic) refinement.[59–61] A previous adaptive parameterization approach using B-spline surface control[59] required the use knot insertion. On the other hand, a new FFD volume can be created with its control points placed completely arbitrarily and therefore more strategically. Of course, the FFD volume itself would change, but the underlying geometry can be re-embedded in this new FFD volume without being modified. The adaptivity can be used to add new FFD control points progressively or simply redistribute them.

V. Conclusions

Two geometry control methods, namely B-spline surface control and FFD control, have been compared with respect to their effectiveness for aerodynamic shape optimization. Both can be used successfully for a wide range of challenging optimization problems. B-spline surface control provides somewhat better local control of the geometry and therefore often leads to slightly lower objective function values. The FFD approach provides several advantages in problem setup for complex geometries as well as a few disadvantages. Overall the results suggest that B-spline surface control is preferred for simple geometries such as wings, while the FFD approach is advantageous for more complex geometries such as unconventional aircraft. Finally,

the generality of the FFD control approach appears to be particularly well suited to a multistart algorithm as well as adaptive and progressive geometry control strategies.

Acknowledgments

The authors gratefully acknowledge the financial assistance from the National Sciences and Engineering Research Council, the Canada Research Chairs program, and the University of Toronto. Computations were performed on the GPC supercomputer at the SciNet HPC Consortium, part of Compute Canada. SciNet is funded by: the Canada Foundation for Innovation under the auspices of Compute Canada, the Government of Ontario, Ontario Research Fund - Research Excellence, and the University of Toronto.

References

[1]Telidetzki, K., Osusky, L., and Zingg, D. W., "Application of Jetstream to a suite of aerodynamic shape optimization problems," *52nd AIAA Aerospace Sciences Meeting*, No. AIAA-2014-0571, National Harbor, Maryland, 2014.

[2]Lee, C., Koo, D., Telidetzki, K., Buckley, H., Gagnon, H., and Zingg, D. W., "Aerodynamic shape optimization of benchmark problems using Jetstream," *53rd AIAA Aerospace Sciences Meeting*, No. AIAA-2015-0262, Kissimmee, Florida, January 2015.

[3]Koo, D. and Zingg, D. W., "Progress in aerodynamic shape optimization based on the Reynolds-averaged Navier-Stokes equations," *54th AIAA Aerospace Sciences Meeting*, No. AIAA-2016-1292, San Diego, California, January 2016.

[4]Meheut, M., Dumont, A., Carrier, G., and Peter, J. E., "Gradient-based optimization of CRM wing-alone and wing-body-tail configurations by RANS adjoint technique," *54th AIAA Aerospace Sciences Meeting*, No. AIAA-2016-1293, San Diego, California, January 2016.

[5]Kenway, G. K. and Martins, J., "Aerodynamic shape optimization of the CRM configuration including buffet-onset conditions," *54th AIAA Aerospace Sciences Meeting*, No. AIAA-2016-1294, San Diego, California, January 2016.

[6]Fabiano, E. and Mavriplis, D. J., "Adjoint-based aerodynamic design on unstructured meshes," *54th AIAA Aerospace Sciences Meeting*, No. AIAA-2016-1295, San Diego, California, January 2016.

[7]Rizzi, A. W., Zhang, M., Bisson, F., and Nadarajah, S., "Comparitive study of two optimization frameworks applied to case III," *54th AIAA Aerospace Sciences Meeting*, No. AIAA-2016-1296, San Diego, California, January 2016.

[8]Ren, J., Thelen, A. S., Amrit, A., Du, X., Leifsson, L. T., Tesfahunegn, Y., and Koziel, S., "Application of multifidelity optimization techniques to benchmark aerodynamic design problems," *54th AIAA Aerospace Sciences Meeting*, No. AIAA-2016-1542, San Diego, California, January 2016.

[9]Masters, D. A., Poole, D. J., Taylor, N. J., Rendall, T. C. S., and Allen, C. B., "Impact of shape parameterization on aerodynamic optimisation of benchmark problem," *54th AIAA Aerospace Sciences Meeting*, No. AIAA-2016-1544, San Diego, California, 2016.

[10]Zhang, Y., Han, Z., Shi, L., and Song, W., "Multi-round surrogate-based optimization for benchmark aerodynamic design problems," *54th AIAA Aerospace Sciences Meeting*, No. AIAA-2016-1545, San Diego, California, January 2016.

[11]Samareh, J. A., "Survey of shape parameterization techniques for high-fidelity multidisciplinary shape optimization," *AIAA Journal*, Vol. 39, No. 5, 2001, pp. 877–884.

[12]Mousavi, A., Castonguay, P., and Nadarajah, S., "Survey of shape parameterization techniques and its effect on three-dimensional aerodynamic shape optimization," *18th AIAA Computational Fluid Dynamics Conference*, No. AIAA-2007-3837, Miami, Florida, 2007.

[13]Castonguay, P. and Nadarajah, S., "Effect of shape parameterization on aerodynamic shape optimization," *45th AIAA Aerospace Sciences Meeting and Exhibit*, No. AIAA-2007-59, Reno, Nevada, 2007.

[14]Anderson, W. K., Karman, S. L., and Burdyshaw, C., "Geometry Parameterization Method for Multidisciplinary Applications," *AIAA Journal*, Vol. 47, No. 6, 2009, pp. 1568–1578.

[15]Gagnon, H. and Zingg, D. W., "Two-level free-form and axial deformation for exploratory aerodynamic shape optimization," *AIAA Journal*, Vol. 53, No. 7, 2015, pp. 2015–2026.

[16]Hicken, J. E. and Zingg, D. W., "Aerodynamic optimization algorithm with integrated geometry parameterization and mesh movement," *AIAA Journal*, Vol. 48, No. 2, 2010, pp. 400–413.

[17]Braibant, V. and Fleury, C., "Shape optimal design using B-splines," *Computer Methods in Applied Mechanics and Engineering*, Vol. 44, No. 3, 1984, pp. 247–267.

[18]Sobieczky, H., "Parametric airfoils and wings," *Notes on Numerical Fluid Mechanics*, Vol. 68, Vieweg, 1998, pp. 71–87.

[19]Samareh, J. A., "Novel multidisciplinary shape parameterization approach," *Journal of Aircraft*, Vol. 38, No. 6, 2001, pp. 1015–1024.

[20]Hicks, R. M. and Henne, P. A., "Wing design by numerical optimization," *Journal of Aircraft*, Vol. 15, No. 7, 1978, pp. 407–412.

[21]Kulfan, B. M. and Bussoletti, J. E., "Fundamental parametric geometry representations for aircraft component shapes," *11th AIAA/ISSMO Multidisciplinary Analysis and Optimization Conference*, No. AIAA-2006-6948, Portsmouth, Virginia, 2006.

[22]Zhu, F. and Qin, N., "Intuitive class/shape function parameterization for airfoils," *AIAA Journal*, Vol. 52, No. 1, 2014, pp. 17–25.

[23]Toal, D. J. J., Bressloff, N. W., and Keane, A. J., "Geometric filtration using proper orthogonal decomposition for aerodynamic design optimization," *AIAA Journal*, Vol. 48, No. 5, 2010, pp. 916–928.

[24]Amoiralis, E. I. and Nikolos, I. K., "Freeform deformation versus B-spline representation in inverse airfoil design," *Journal of Computing and Information Science in Engineering*, Vol. 8, No. 2, 2008.

[25]Masters, D. A., Taylor, N. J., Rendall, T. C. S., Allen, C. B., and Pool, D. J., "A geometric comparison of aerofoil shape parameterisation methods," *54th AIAA Aerospace Sciences Meeting*, No. AIAA-2016-0558, San Diego, California, 2016.

[26]Campbell, R. L., "An approach to constrained aerodynamic design with application to airfoils," *NASA Tech. Report*, 1992.

[27]Farin, G. E., *Curves and surfaces for computer-aided geometric design: A practical code*, Academic Press, Inc., 1996.

[28]Sederberg, T. W. and Parry, S. R., "Free-form deformation of solid geometric models," *13th Annual Conference on Computer Graphics and Interactive Techniques*, No. 4, Dallas, Texas, 1986, pp. 151–160.

[29]Ghoman, S. S., Wang, Z., Chen, P. C., and Kapania, R. K., "A POD-based reduced order design scheme for shape optimization of air vehicles," *53rd AIAA/ASME/ASCE/AHS/ASC Structures, Structural Dynamics and Materials Conference*, No. AIAA-2012-1808, Honolulu, Hawaii, 2012.

[30]Poole, D. J., Allen, C. B., and Rendall, C. S., "Metric-based mathematical derivation of efficient airfoil design variables," *AIAA Journal*, Vol. 53, No. 5, 2015, pp. 1349–1361.

[31]Drela, M., "XFOIL: An analysis and design system for low Reynolds number airfoils," *Low Reynolds number aerodynamics*, Springer, 1989, pp. 1–12.

[32]Nemec, M. and Zingg, D. W., "Newton-Krylov algorithm for aerodynamic design using the Navier-Stokes equations," *AIAA Journal*, Vol. 40, No. 6, 2002, pp. 1146–1154.

[33]Lyu, Z., Kenway, G. K. W., and Martins, J. R. R. A., "Aerodynamic Shape Optimization Investigations of the Common Research Model Wing Benchmark," *AIAA Journal*, Vol. 53, No. 4, 2015, pp. 968–985.

[34]Duvigneau, R., "Adaptive parameterization using free-form deformation for aerodynamic shape optimization," Tech. rep., INRIA, France, July 2006.

[35]Anderson, G. R., Aftosmis, M. J., and Nemec, M., "Constraint-based shape parameterization for aerodynamic design," *7th International Conference on Computational Fluid Dynamics*, No. ICCFD7-2001, Big Island, Hawaii, July 2012.

[36]Amoignon, O., Navrátil, J., and Jiří, H., "Study of parameterizations in the project CEDESA," *52nd AIAA Aerospace Sciences Meeting*, No. AIAA-2014-0570, National Harbor, Maryland, January 2014.

[37]Gagnon, H. and Zingg, D. W., "Two-level free-form deformation for high-fidelity aerodynamic shape optimization," *12th AIAA Aviation Technology, Integration, and Operations (ATIO) Conference and 14th AIAA/ISSMO Multidisciplinary Analysis and Optimization Conference*, No. AIAA-2012-5447, Indianapolis, Indiana, September 2012.

[38]Gagnon, H. and Zingg, D. W., "Euler-equation-based drag minimization of unconventional aircraft configurations," *Journal of Aircraft,* Published online, DOI: 10.2514/1.C033591, 2016.

[39]Gagnon, H. and Zingg, D. W., "Aerodynamic trade study of a box-wing aircraft configuration," *Journal of Aircraft* Published online, DOI: 10.2514/1.C033592, 2016.

[40]Osusky, L., Buckley, H., Reist, T., and Zingg, D. W., "Drag minimization based on the Navier-Stokes equations using a Newton-Krylov approach," *AIAA Journal*, Vol. 53, No. 6, 2015, pp. 1555–1577.

[41]Gagnon, H. and Zingg, D. W., "Geometry generation of complex unconventional aircraft with application to high-fidelity aerodynamic shape optimization," *21st AIAA Computational Fluid Dynamics Conference*, No. AIAA-2013-2850, San Diego, California, 2013.

[42]Lazarus, F., Coquillart, S., and Jancène, P., "Axial deformations: an intuitive deformation technique," *Computer-Aided Design*, Vol. 26, No. 8, 1994, pp. 607–613.

[43]Truong, A. H., Oldfield, C. A., and Zingg, D. W., "Mesh movement for a discrete-adjoint Newton-Krylov algorithm for aerodynamic optimization," *AIAA Journal*, Vol. 46, No. 7, 2008, pp. 1695–1704.

[44]Hicken, J. E. and Zingg, D. W., "Parallel Newton-Krylov solver for the Euler equations discretized using simultaneous-approximation terms," *AIAA Journal*, Vol. 46, No. 11, 2008, pp. 2773–2786.

[45]Osusky, M. and Zingg, D. W., "A parallel Newton-Krylov-Schur flow solver for the Navier-Stokes equations discretized using summation-by-parts operators," *AIAA Journal*, Vol. 51, No. 12, 2013, pp. 2833–2851.

[46]Jameson, A., Schmidt, W., and Turkel, E., "Numerical solutions of the Euler equations by finite volume methods using Runge-Kutta time-stepping schemes," *14th Fluid and Plasma Dynamics Conference*, No. AIAA-81-1259, Palo Alto, California, 1981.

[47]Pulliam, T. H. and Zingg, D. W., *Fundamental algorithms in computational fluid dynamics*, Scientific computation, Springer International Publishing, 2014.

[48]Swanson, R. C. and Turkel, E., "On central-difference and upwind schemes," *Journal of Computational Physics*, Vol. 101, No. 2, 1992, pp. 292–306.

[49]Chernukhin, O. and Zingg, D. W., "Multimodality and global optimization in aerodynamic design," *AIAA Journal*, Vol. 51, No. 6, 2013, pp. 1342–1354.

[50]Nocedal, J. and Wright, S., *Numerical optimization*, Springer series in operations research and financial engineering, Springer-Verlag New York, 1999.

[51]De Sturler, E., "Nested Krylov methods based on GCR," *Journal of Computational and Applied Mathematics*, Vol. 67, No. 1, 1996, pp. 15–41.

[52]De Sturler, E., "Truncation strategies for optimal Krylov subspace methods," *SIAM Journal of Numerical Analysis*, Vol. 36, No. 3, 1999, pp. 864–889.

[53]Hicken, J. E. and Zingg, D. W., "A simplified and flexible variant of GCROT for solving nonsymmetric linear systems," *SIAM Journal on Scientific Computing*, Vol. 32, No. 3, 2010, pp. 1672–1694.

[54]Gill, P. E., Murray, W., and Saunders, M. A., "SNOPT: An SQP algorithm for large-scale constrained optimization," *SIAM Review*, Vol. 47, No. 1, 2005, pp. 99–131.

[55]Hicken, J. E. and Zingg, D. W., "Induced drag minimization of nonplanar geometries based on the Euler Equations," *AIAA Journal*, Vol. 48, No. 11, 2010, pp. 2564–2575.

[56]Levy, D., Laflin, K., Tinoco, E., Vassberg, J., Mani, M., Rider, B., Rumsey, C., Wahls, R., Morrison, J., Brodersen, O., Crippa, S., Mavriplis, D., and Murayama, M., "Summary of data from the Fifth AIAA CFD Drag Prediction Workshop," *51st AIAA Aerospace Sciences Meeting*, Dallas, Texas, January 2013.

[57]Reist, T. A. and Zingg, D. W., "Aerodynamic design of regional-class blended wing-body aircraft through high-fidelity aerodynamic shape optimization," *Journal of Aircraft,* (Submitted), 2016.

[58]Destarac, D., Carrier, G., Anderson, G. R., Nadarajah, S., Poole, D. J., Vassberg, J. C., and Zingg, D. W., "Uniform post-processing of ADO-DG-NACA0012-Euler Optimized Shapes," In preparation.

[59]Han, X. and Zingg, D. W., "An adaptive geometry parameterization for aerodynamic shape optimization," *Optimization and Engineering*, Vol. 15, No. 1, 2014, pp. 69–91.

[60]Anderson, G. R. and Aftosmis, M. J., "Adaptive shape control for aerodynamic design," *56th AIAA/ASCE/AHS/ASC Structures, Structural Dynamics, and Materials Conference*, No. AIAA-2015-0398, Kissimmee, Florida, January 2015.

[61]Anderson, G. R., Nemec, M., and Aftomis, M. J., "Aerodynamic shape optimization benchmarks with error control and automatic parameterization," *53rd AIAA Aerospace Sciences Meeting*, No. AIAA-2015-1719, Kissimmee, Florida, January 2015.

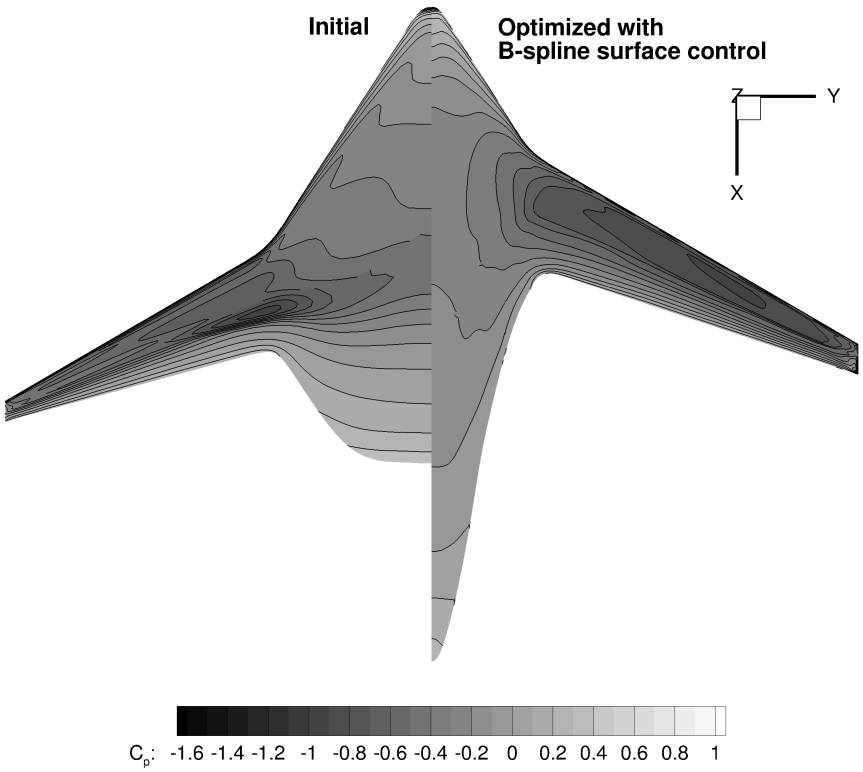

(a) Initial and B-spline control

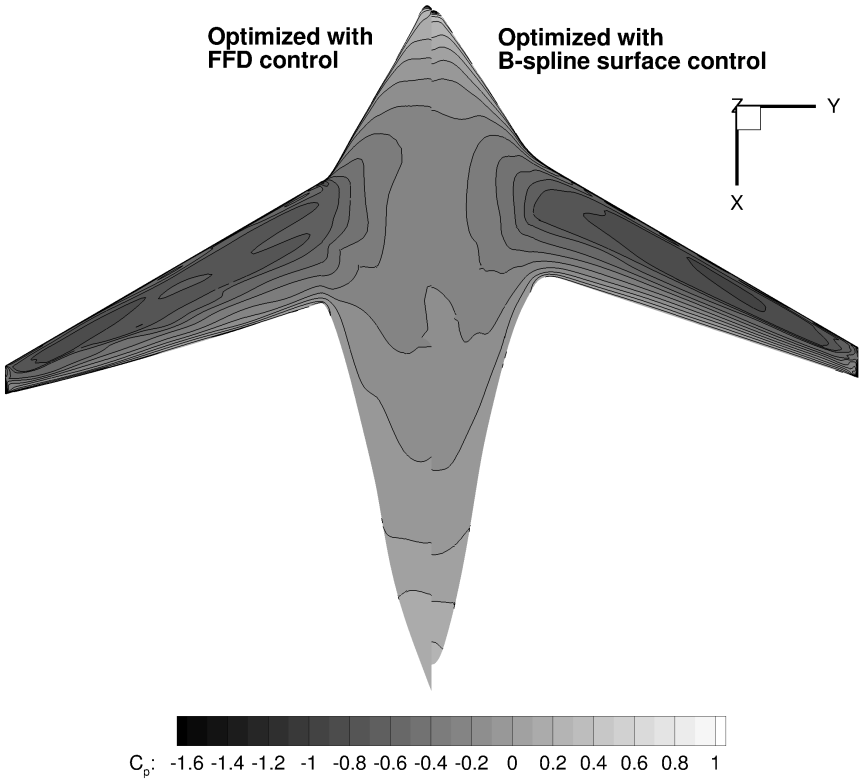

(b) FFD and B-spline control

Figure 11: Case 3 - Upper surface pressure contours for initial and optimized BWBs using B-spline surface and FFD control computed on fine mesh

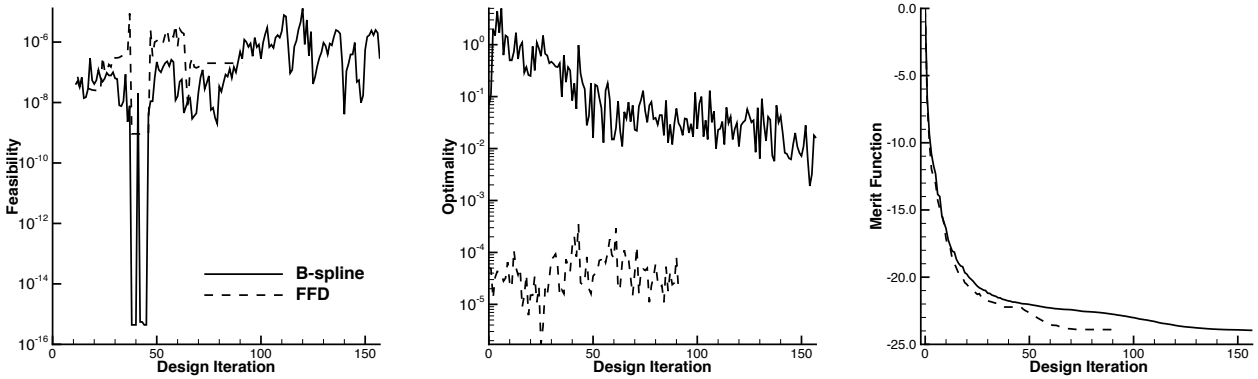

Figure 12: Case 3 - SNOPT convergence for BWB optimizations